Annual Heat Balance of Martian Polar Caps: Viking Observations

David A. Paige; Andrew P. Ingersoll

Science, New Series, Vol. 228, No. 4704 (Jun. 7, 1985), 1160-1168.

ticidal Value, a Review of the Literature Up to 1941 (E-661, U.S. Department of Agriculture–Agricultural Research Administration , Bureau of Entomology and Plant Quarantine, Washington, D.C., 1945).
28. F. Matsumura, *Toxicology of Insecticides* (Plenum, New York, 1975); L. M. Schoonhoven, *Recent Adv. Phytochem.* **5**, 197 (1972); *Chemistry and World Food Supplies: Research Priorities for Development* (National Academy Press, Washington, D.C., 1982); D. M. Secoy and A. E. Smith, *Econ. Bot.* **37**, 28 (1983).
29. L. W. Levy, *Environ. Exp. Bot.* **21**, 389 (1981).
30. V. E. Tyler, L. R. Brady, J. E. Robbers, *Pharmacognosy* (Lea and Febiger, Philadelphia, ed. 7, 1976), pp. 490–509.
31. B. Gilbert, in *Natural Products and the Protection of Plants*, G. B. Marini-Bettolo, Ed. (Elsevier, New York, 1977), pp. 225–246.
32. I. Schmeltz, in *Naturally Occurring Insecticides*, M. Jacobson and D. G. Crosby, Eds. (Dekker, New York, 1971), pp. 99–136.
33. H. Gysin, *Chimia* **8**, 205 (1954); E. Stedman, *Biochem. J.* **20**, 719 (1926).
34. L. E. Gregory, *Amer. J. Bot.* **68**, 586 (1981); W. J. Meudt and M. J. Thompson, *Proc. Plant Growth Regulator Soc. Am.* **10**, 306 (1983); W. J. Meudt, M. J. Thompson, H. W. Bennett, *ibid.*, p. 312.
35. J. D. Cohen and W. J. Meudt, *Plant Physiol.* **72**, 691 (1983).
36. S. von Reis Altschul, *Sci. Am.* **236**, 96 (May 1977); *Drugs and Foods from Little-Known Plants* (Harvard Univ. Press, Cambridge, Mass., 1973).
37. M. Suffness and J. Douros, *J. Nat. Prod.* **45**, 1 (1982); E. Frei III, *Science* **217**, 600 (1982).
38. O. R. Gottlieb and W. B. Mors, *J. Agric. Food Chem.* **28**, 196 (1980).
39. V. H. Heywood, *Pure Appl. Chem.* **34**, 355 (1973); K. Larsen and L. B. Holm-Nielsen, Eds., *Tropical Botany* (Academic Press, New York, 1979); N. Myers, *The Sinking Ark* (Pergamon, New York, 1979); *Conversion of Tropical Moist Forests* (National Academy of Sciences, Washington, D.C. 1980); P. H. Raven, *Bull. Entomol. Soc. Am.* **29**, 4 (1983); *Technologies to Sustain Tropical Forest Resources* (OTA-F-214, Office of Technology Assessment, Washington, D.C., 1984).
40. V. E. Tyler, *Econ. Bot.* **33**, 377 (1979).
41. C. Djerassi, C. Shih-Coleman, J. Diekman, *Science* **186**, 596 (1974); J. J. Menn, *J. Agric. Food Chem.* **28**, 2 (1980).
42. L. M. Schoonhoven, *Entomol. Exp. Appl.* **31**, 57 (1982); K. Nakanishi, in *Insect Biology in the Future*, M. Locke and D. S. Smith, Eds. (Academic Press, New York, 1980), pp. 603–612; *Recent Adv. Phytochem.* **9**, 283 (1974).
43. H. Schmutterer, K. R. S. Ascher, H. Rembold, Eds., *Natural Pesticides from the Neem Tree (*Azadirachta indica A. Juss*)* (German Agency for Technical Cooperation, Eschborn, Germany, 1980); J. D. Warthen, Jr., Azadirachta indica*: A Source of Insect Feeding Inhibitors and Growth Regulators* (U.S. Department of Agriculture–Science and Education Administration, Beltsville, Md., 1979).
44. R. C. Saxena, in *Chemistry and World Food Supplies: The New Frontiers*, L. W. Shemilt, Ed. (Pergamon, New York, 1983), pp. 143–161.
45. J. A. Klocke, thesis, University of California, Berkeley (1982).
46. K. Nakanishi, in *Natural Products and the Protection of Plants*, G. B. Marini-Bettolo, Ed. (Elsevier, New York, 1977), pp. 185–210.
47. G. B. Staal, *Annu. Rev. Entomol.* **20**, 417 (1975).
48. W. S. Bowers, in *The Juvenile Hormones*, L. I. Gilbert, Ed. (Plenum, New York, 1976), pp. 394–408; in *Insecticide Mode of Action*, J. R. Coates, Ed. (Academic Press, New York, 1982), pp. 403–427.
49. D. P. Carew and E. J. Staba, *Lloydia* **28**, 1 (1965); E. J. Staba, *Recent Adv. Phytochem.* **2**, 75 (1969); Z. Puhan and S. M. Martin, *Prog. Ind. Microbiol.* **9**, 13 (1971); W. Barz, E. Reinhard, M. H. Zenk, Eds., *Plant Tissue Culture and Its Bio-technological Application* (Springer-Verlag, New York, 1977); D. N. Butcher, in *Plant Cell, Tissue, and Organ Culture*, J. Reinert and Y. P. S. Bajaj, Eds. (Springer-Verlag, New York, 1977), pp. 668–693; M. W. Fowler, *Pharm. J.* **224**, 39 (1980); E. J. Staba, *Plant Tissue Culture as a Source of Biochemicals* (CRC Press, Boca Raton, Fla., 1980); D. Aviv *et al.*, *Planta Med.* **42**, 236 (1981); J. Stockigt, K. H. Pawelka, T. Tanahashi, B. Danieli, W. E. Hull, *Helv. Chim. Acta* **66**, 2525 (1983); F. Sato and Y. Yamada, *Phytochemistry* **23**, 281 (1984).
50. Board on Science and Technology for International Development, *Priorities in Biotechnology Research for International Development* (National Academy Press, Washington, D.C., 1982), pp. 137–138.
51. J. Berlin, *Endeavour* **8**, 5 (1984); M. L. Shuler, J. W. Pyne, G. A. Hallsby, *J. Am. Oil Chem. Soc.* **61**, 1724 (1984).
52. M. L. Shuler, *Ann. N.Y. Acad. Sci.* **369**, 65 (1981); H. E. Street, in *Plant Cell, Tissue and Organ Culture*, J. Reinert, Y. P. S. Bajaj, Eds. (Springer-Verlag, New York, 1977), pp. 649–667; O. P. Sahai and M. L. Shuler, *Biotechnol. Bioeng.* **26**, 111 (1983); M. M. Yeoman, M. B. Miedzybrodzka, K. Lindsey, W. R. McLauchlan, in *Plant Cell Cultures, Results and Perspectives*, F. Sala, B. Parisi, R. Cella, O. Cifferi, Eds. (Elsevier, New York, 1980), pp. 327–343.
53. W. Barz and B. E. Ellis, in *Natural Products as Medicinal Agents*, J. L. Beal and E. Reinhard, Eds. (Hippokrates, Stuttgart, Germany, 1981), pp. 471–507.
54. E. J. Staba, in *Plant Tissue Culture 1982*, A. Fujiwara, Ed. (Maruzen, Tokyo, Japan, 1982), pp. 25–30.
55. M. Tabata, T. Ogino, K. Yoshioka, N. Yoshikawa, N. Hiraoka, in *Frontiers of Plant Tissue Culture*, T. A. Thorpe, Ed. (Univ. of Calgary Press, Calgary, 1978), pp. 213–222.
56. F. Sasse, U. Heckenberg, J. Berlin, *Plant Physiol.* **69**, 400 (1982).
57. R. S. Chaleff, *Science* **219**, 676 (1983); *Genetics of Higher Plants: Applications of Cell Culture* (Cambridge Univ. Press, New York, 1981).
58. A. W. Alfermann and E. Reinhard, unpublished data; see (*53*).
59. P. F. Heinstein, in *Plant Tissue Culture 1982*, A. Fujiwara, Ed. (Maruzen, Tokyo, Japan, 1982), pp. 675–676.
60. K. K. Kamo, W. Kimoto, A. F. Hsu, P. G. Mahlberg, D. D. Bills, *Phytochemistry* **21**, 219 (1982).
61. K. Hahlbrock, in *The Biochemistry of Plants*, E. E. Conn, Ed. (Academic Press, New York, 1981), vol. 7, pp. 425–456; D. N. Kuhn, J. Chappell, A. Boudet, K. Hahlbrock, *Proc. Natl. Acad. Sci. U.S.A.* **8**, 1102 (1984).
62. B. J. Nikolau, E. S. Wurtele, P. K. Stumpf, *Plant Physiol.* **75**, 979 (1984).
63. W. Barz and J. Koster, in *The Biochemistry of Plants*, P. K. Stumpf and E. E. Conn, Eds. (Academic Press, New York, 1981), vol. 7, pp. 35–80.
64. M. H. Zenk, in *Frontiers of Plant Tissue Culture*, T. A. Thorpe, Ed. (Univ. of Calgary, Calgary, 1978), pp. 1–13.
65. D. E. Eveleigh, *Sci. Am.* **245**, 154 (March 1981).

RESEARCH ARTICLE

Annual Heat Balance of Martian Polar Caps: Viking Observations

David A. Paige and Andrew P. Ingersoll

One of the most interesting results of the Viking mission to Mars was the discovery that the seasonal behavior of CO_2 frost at the Martian poles is not symmetric. In the north, the Viking orbiter summertime observations gave strong evidence for an exposed and permanent water ice polar cap, and the absence of solid CO_2 (*1, 2*). In the south, the observations suggest that solid CO_2 remained on the surface through the end of the summer season (*3, 4*). These results were not expected, and have important implications for our understanding of the Martian climate system.

On Mars, the temperatures of CO_2 frost deposits are determined by the local partial pressure of CO_2 gas, the dominant constituent of the Martian atmosphere. The partitioning of total available CO_2 between atmosphere and polar caps over climatic time scales is determined by the vapor pressures of the coldest permanent year-long CO_2 deposits on the planet (*5, 6*). Since the temperatures of stable CO_2 frost deposits are governed by their annual heat balance, the properties and processes that determine the annual heat balance at the Martian poles have a major impact on the composition and mass of the Martian atmosphere (*7*). Since both poles receive the same total insolation (sunlight incident at the top of the atmosphere) during a year, the present north-south asymmetry in the behavior of CO_2 frost shows that processes generated on Mars itself must play an important role in determining the behavior of the Martian polar caps over climatic time scales. Identifying and understanding these processes will be an important step toward understanding the past and present climate of Mars.

We present here an extensive compilation of Viking Infrared Thermal Mapper (IRTM) solar reflectance and infrared emission observations of the Martian north and south polar regions. The observations span an entire Mars year, and are used to determine annual radiation budgets and heat budgets for the core regions of the north and south permanent or residual polar caps. The results define the current behavior of CO_2 frost at the

David A. Paige is a graduate student in planetary science and Andrew P. Ingersoll is professor of planetary science in the Division of Geological and Planetary Sciences, California Institute of Technology, Pasadena 91125.

Abstract. *The Infrared Thermal Mappers aboard the two Viking orbiters obtained solar reflectance and infrared emission measurements of the Martian north and south polar regions during an entire Mars year. The observations were used to determine annual radiation budgets, infer annual carbon dioxide frost budgets, and constrain spring season surface and atmospheric properties with the aid of a polar radiative model. The results provide further confirmation of the presence of permanent CO_2 frost deposits near the south pole and show that the stability of these deposits can be explained by their high reflectivities. In the north, the observed absence of solid CO_2 during summer was primarily the result of enhanced CO_2 sublimation rates due to lower frost reflectivities during spring. The results suggest that the present asymmetric behavior of CO_2 frost at the Martian poles is caused by preferential contamination of the north seasonal polar cap by atmospheric dust.*

Martian poles and provide new clues to the properties and processes that may be responsible for this behavior.

Polar heat balance. The basic principle that underlies heat balance studies is that the total net flux of energy into a system through its boundaries is equal to the rate at which energy is stored inside the system. The systems chosen for this study consist of the atmospheres and seasonal frost deposits within two small regions that correspond geographically to the core areas on the Martian residual polar caps. Figure 1 shows the boundaries of these north and south study regions superposed on the approximate areas of the residual polar caps. The instantaneous heat balance equation for the seasonal frost deposits and atmospheres within either of these regions per unit area can be written

$$F_{\mathrm{Rad}} + F_{\mathrm{Horiz}} + F_{\mathrm{Cond}} = S_{\mathrm{Atm}} + S_{\mathrm{CO_2}} \quad (1)$$

where F_{Rad} is the net flux of solar and infrared radiation into the regions at the top of the atmosphere; F_{Horiz} is the net horizontal flux of sensible and latent heat into the regions at their boundaries; F_{Cond} is the upward subsurface conductive heat flux into the regions at the top boundaries of the underlying permanent polar caps; S_{Atm} is the rate of total potential energy storage in the atmospheric columns within the regions; and $S_{\mathrm{CO_2}}$ is the rate of latent heat storage in condensing or sublimating CO_2 condensates within the regions. Measures of kinetic energy generation, latent heat storage in H_2O condensates, and heat flow from the Martian interior are not included in Eq. 1 because the magnitudes are much smaller than the terms included. The relevance of the heat balance equation to the behavior of seasonal frosts within the north and south study regions lies in the CO_2 latent heat storage term, which can be written

$$S_{\mathrm{CO_2}} = -L_{\mathrm{CO_2}} \frac{dM_{\mathrm{CO_2}}}{dt} \quad (2)$$

$L_{\mathrm{CO_2}}$ is the latent heat of sublimation of CO_2, and $dM_{\mathrm{CO_2}}/dt$ is the net rate of solid CO_2 accumulation within the boundaries of the study regions. The instantaneous heat balance equation can be solved to yield $S_{\mathrm{CO_2}}$ if all the other terms in the equation can be determined.

Radiation budget measurements. The dominant measurable quantity in Eq. 1 is F_{Rad}, which can be written

$$F_{\mathrm{Rad}} = F_{\mathrm{Solar}} (1 - A_{\mathrm{P}}) - F{\uparrow}_{\mathrm{IR}} \quad (3)$$

where F_{Solar} is the flux of incident solar radiation at the top of the atmosphere corrected for the cosine of the solar zenith angle; A_{P} is the planetary albedo or the total combined reflectivity of the surface and atmosphere; $F{\uparrow}_{\mathrm{IR}}$ is the outward flux of emitted radiation at all wavelengths at the top of the atmosphere. Since the north and south study regions experience no significant diurnal variations in insolation, their thermal and reflectance properties are purely seasonal. This makes them significantly easier targets for satellite radiation balance measurements than other regions of the planet.

The IRTM instruments aboard the two Viking orbiters obtained sufficient spectral, temporal, and angular coverage to determine F_{Rad} for the north and south study regions with reasonable accuracy and excellent time resolution throughout a Martian year. The instruments operated in six wavelength bands including a broad-band solar reflectance channel (λ = 0.3 to 3 μm) and five broad infrared channels ($\lambda \approx$ 7, 9, 11, 15, and 20 μm). During clear atmospheric conditions, the 7-, 9-, 11- and 20-μm channels measured surface brightness temperatures. The 15-μm channel, with spectral response centered on a strong CO_2 absorption feature, measured atmospheric temperatures over a broad range of altitudes with maximum sensitivity near the 0.6-mbar pressure level (*8*).

The observing geometry for single IRTM observations can be characterized by three angles, φ, θ, and ψ, where φ is the incidence angle measured from the local zenith to the sun, θ is the emission angle measured from the local zenith to the spacecraft, and ψ is the solar azimuth angle or the projected angle from the sun to the spacecraft measured on the local planet tangent plane. The IRTM's obtained more than 250,000 separate observations within the boundaries of the study regions for a wide range of observing geometries. The full-width at half maximum fields of view, or spot diameters, of single IRTM observations that were used varied widely but always corresponded to less than 2° of latitude on the planet near the poles.

Figures 2, A and B, and 3, A and B, are partial compilations of the IRTM infrared emission and solar reflectance measurements of the north and south study regions. They are intended to show the general character of the data with a minimum of processing. These parts of the figures were constructed by discarding observations that were obtained at emission angles greater than 60°

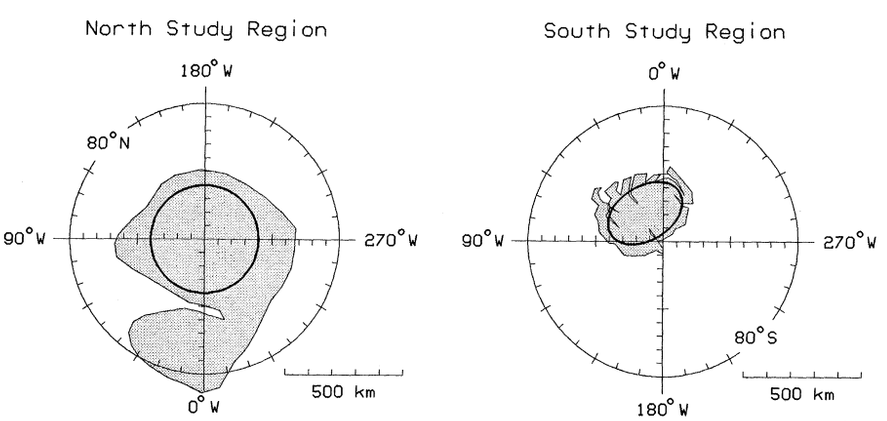

Fig. 1. Maps showing the boundaries of the study regions superposed on the approximate areas of the Martian north (left) and south (right) polar caps as they appear during the late summer seasons (shaded).

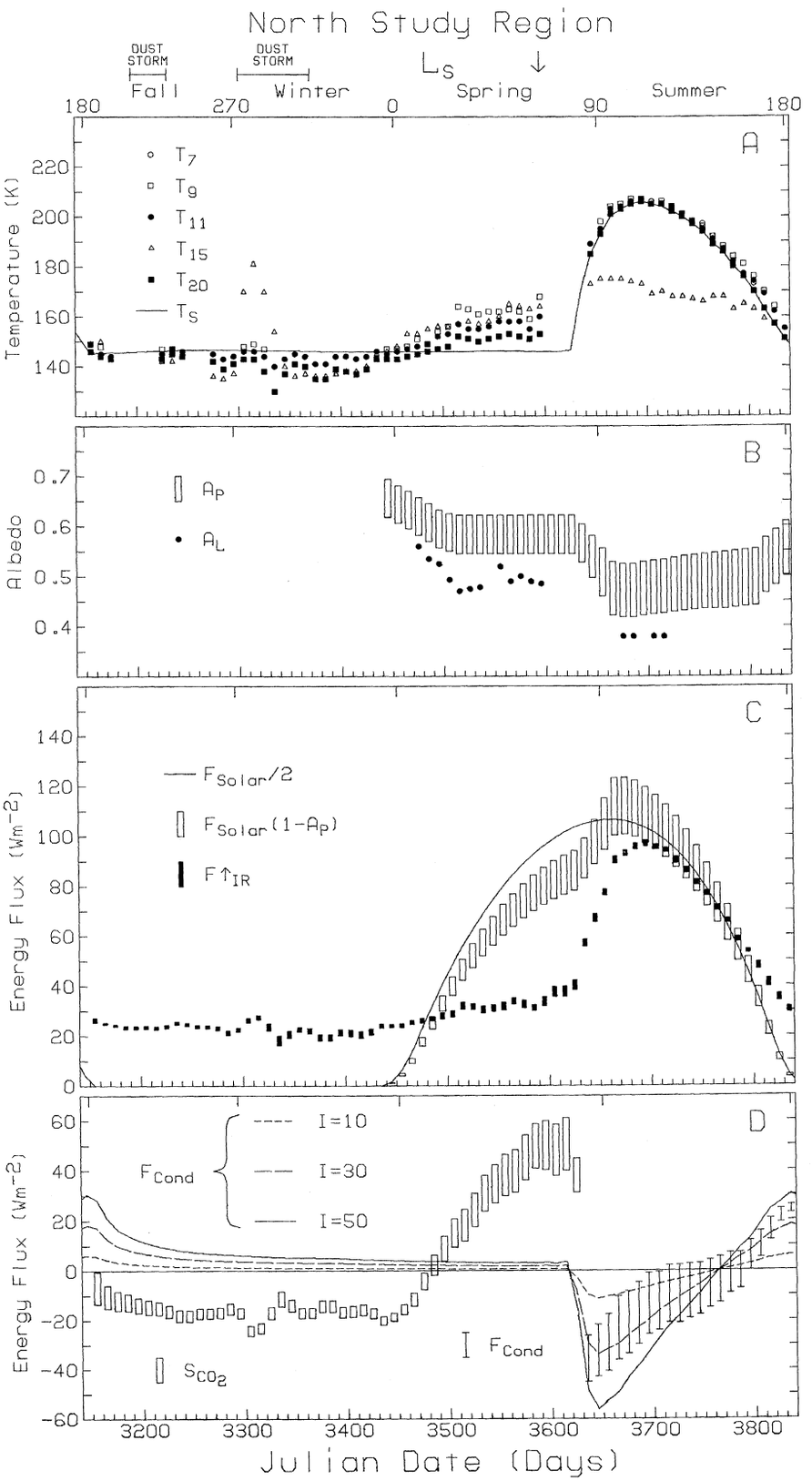

Fig. 2. The IRTM observations and heat balance quantities for the north study region for one Mars year. (A) Brightness temperatures T_7, T_9, T_{11}, T_{15}, and T_{20} for emission angle $\theta \leq 60°$ and surface temperature estimates T_S. (B) Lambert albedos A_L for $\theta \leq 30°$ and upper and lower limits for planetary albedos A_P. (C) Radiation budget quantities at the top of the atmosphere. Insolation rates F_{Solar} and upper and lower limits for solar absorption rates $F_{Solar}(1 - A_P)$ and emission $F\uparrow_{IR}$. (D) Upper and lower limits for derived CO_2 latent heat storage rates S_{CO_2} and calculated upward subsurface conductive heat fluxes F_{Cond}.

for brightness temperatures and 30° for solar reflectances to reduce the effects of varying spacecraft viewing geometries. The remaining data were binned, averaged, and then plotted with 10-day time resolution. The abscissa scales are Julian date in days measured from 12 hours (Universal Time) on 23 May 1968 and L_s, the areocentric longitude of the sun, an angular measure of Martian season measured from spring equinox in the north. The south polar winter data were obtained before the spring data. Figures 2A and 3A show radiance-weighted average brightness temperatures in the IRTM infrared channels designated T_7, T_9, T_{11}, T_{20}. Figures 2B and 3B show averaged IRTM solar reflectances in terms of Lambert albedo, which is the ratio of the measured reflected intensity at a given observing geometry to the intensity that would be obtained if the study regions were ideal, perfectly reflecting, uniformly diffusing surfaces. Gaps in the data are the result of incomplete coverage of the study regions at the specified observing geometries and times. The 7- and 9-μm channel data were not plotted during most of the fall and winter seasons because of low signal-to-noise ratios for T_7 below 165 K and T_9 below 147 K. The approximate durations of two Martian great dust storms that occurred during 1977 are also shown.

Upper and lower limits for $F\uparrow_{IR}$ for the north and south study regions are shown in Figs. 2C and 3C. They were determined by first separating all the 10-day averaged radiances in the five IRTM infrared channels into two emission angle bins; $0° \leq \theta < 60°$ and $60° \leq \theta < 90°$. Standard deviations for the radiances within each bin were generally the equivalent of ~3 K whereas differences between the average temperatures in the high and low emission angle bins ranged from 0 to ~10 K. An empirical spectral model was used to synthesize complete emission spectra by computing brightness temperatures at all wavelengths from linear combinations of the equivalent average brightness temperatures in the two emission angle bins (*9*). Uncertainties in $F\uparrow_{IR}$ are primarily due to potential variations in the unmeasured emission spectrum at wavelengths beyond the sensitivity of the IRTM 20-μm channel. In order to account for these uncertainties, brightness temperatures for $\lambda > 30$ μm were assumed to be bracketed by $T_{20} \pm (T_{11} - T_{20})$, thus making $F\uparrow_{IR}$ most uncertain during periods of high spectral contrasts. The upper and lower limits for the emission rates of the north and south study regions shown in Figs. 2C and 3C contain additional ±1

percent uncertanties for absolute calibration.

Solar absorption rates are more difficult to determine than emission rates because of the complex geometries of reflected radiation fields. The instantaneous planetary albedo is the measured Lambert albedo averaged over the emission hemisphere.

$$A_P = \frac{1}{\pi} \int_0^{2\pi} \int_0^{\pi/2} [A_L(\theta, \psi) \cos\theta \sin\theta \, d\theta \, d\psi] \quad (4)$$

where $A_L(\theta, \psi)$ is the Lambert albedo at a particular emission angle and azimuth angle. Time-dependent planetary albedos for the study regions were determined by constructing bidirectional reflectance plots of successive groups of approximately 40 days of IRTM Lambert albedo measurements as a function of θ and ψ. The plots were hand-contoured and then averaged according to Eq. 4 to yield planetary albedos. The reflected radiation fields were assumed to be bilaterally symmetric. Figure 4 shows late springtime bidirectional reflectance plots for the north and south study regions and a bidirectional reflectance plot for aged terrestrial snow that was measured at a comparable solar zenith angle (*10*) and normalized to $A_P = 0.6$. The angular coverage obtained by the IRTM's was never complete but was usually sufficient to define the bidirectional reflectance of the study regions such that A_P could be estimated with few ambiguities. To estimate the potential uncertainties in A_P during those 40-day periods in which the angular coverage was marginal, the available data were contoured twice, once to yield a minimum A_P and once to yield a maximum A_P. During the most marginal periods, the assumed bidirectional reflectance patterns ranged from nearly isotropic to the most specular observed. Uncertanties in A_P are further compounded by ±5 percent uncertainties in the absolute calibrations of the IRTM solar reflectance channels. Figures 2B and 3B show upper and lower limits for the planetary albedos of the north and south regions.

Figures 2C and 3C show F_{Solar} for the north and south study regions, computed at their average latitudes for a solar constant of 1370 W m^{-2} at 1 AU. The curves are not symmetric because Mars' orbit is eccentric. Perihelion passage currently occurs about 31 days before summer solstice in the south, causing the sunlit seasons in the south to be shorter but more intense than those in the north. The annually averaged insolation rates for both study regions are essentially identical. Upper and lower limits for the solar absorption rates for the study regions are shown in the same figures. Upper and lower limits for F_{Rad} were determined by assuming that the uncertainties in the solar absorption and infrared emission rates were additive.

Smaller heat balance quantities. The rest of the terms in the heat balance equation must be determined by less direct means. This is not as serious as it might sound, since near the Martian poles, the magnitudes of S_{Atm}, F_{Horiz},

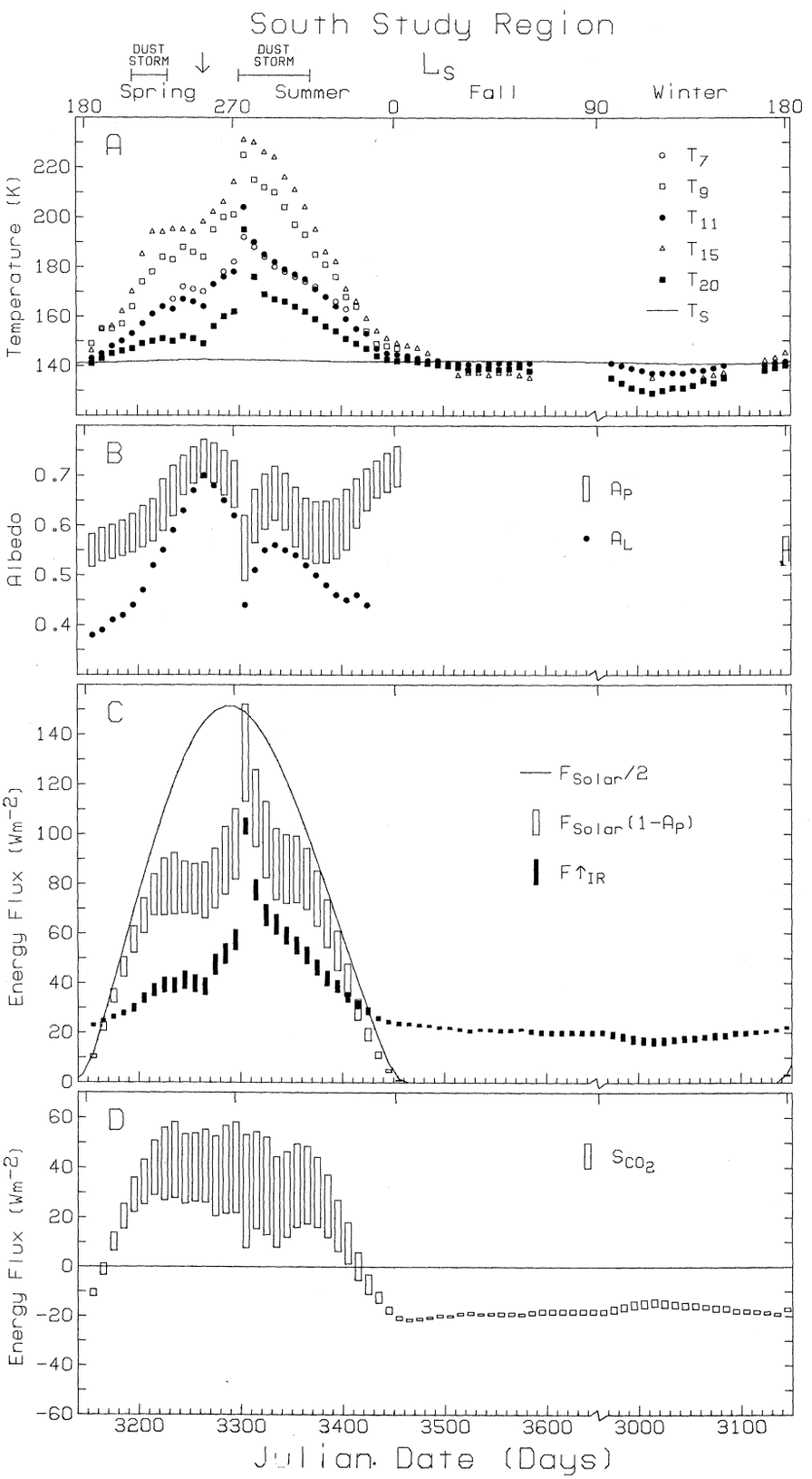

Fig. 3. Same measurements as Fig. 2 but for the south study region (F_{Cond} = 0).

and F_{Cond} are generally much smaller than those of F_{Rad} and S_{CO_2}, which are of order 20 W m^{-2}. This makes proportionately larger uncertainties in the smaller terms almost always less important than uncertainties in the radiation budget measurements for determining CO_2 latent heat storage rates for the study regions.

The smallest and easiest of the three small terms to estimate is S_{Atm}, the atmospheric total potential energy storage rate. The total potential energy of an atmospheric column is the sum of its internal thermal and gravitational potential energies (*11*). To estimate S_{Atm}, the atmospheric columns within the boundaries of the study regions were assumed to be hydrostatic with constant surface pressures of 4.64 mbar in the north and 2.54 mbar in the south. The surface pressures are from estimates of surface frost temperatures that will be presented later. Changes in atmospheric temperatures at all levels were assumed to be equal to the measured changes in T_{15}. The calculated magnitudes of S_{Atm} were typically less than 0.5 W m^{-2}, and never exceeded 3 W m^{-2} (*12*).

A more difficult term to estimate is F_{Horiz}, the instantaneous net horizontal heat flux into the study regions at their boundaries. The results of general circulation model (GCM) calculations show that although the Martian atmosphere is expected to transport some heat from lower, warmer latitudes to the polar regions, the effects of dynamic heat transport on the current heat balance at the Martian poles are small when compared to those of radiation. Martian GCM calculations for seasons near $L_s = 270$, $L_s = 0$ (*13*), and $L_s = 90$ (*14*) all give vertically integrated polar atmospheric advective heating rates ranging from 0 to 10 W m^{-2} (*15*).

The annually averaged upper and lower limits for F_{Rad} are approximately +3 and −7 W m^{-2} for both the north and the south study regions. If one assumed that each region behaved identically from year to year, then the annually averaged values of F_{Cond}, S_{Atm}, and S_{CO_2} would be 0 and the annually averaged value of F_{Horiz} would be 2 ± 5 W m^{-2} from Eq. 1. The assumption of exact year to year repeatability may not be completely correct because although comparisons between the IRTM northern summer observations used in this study and those from one Mars year earlier (*1*) show no discernible interannual variations in thermal or reflectance behavior, orbiter images do show small interannual variations in the extent of CO_2 frost cover near the south pole during summer (*4*).

For the purpose of estimating S_{CO_2}, F_{Horiz} will be assumed to equal 2 W m^{-2} for both study regions throughout the year. Although this procedure may introduce significant uncertainties during some seasons, it is the simplest and least ad hoc method of correcting the instantaneous heat budget results for the assumed minor effects of atmospheric heat transport (*16*). Any effects that this assumption may have on subsequent results will be discussed.

Subsurface heat conduction. The last term in the heat balance equation to consider is F_{Cond}, the upward subsurface conductive heat flux at the top boundaries of the permanent caps. It will be useful to first consider the case of the north study region.

The relative magnitudes of seasonal variations in F_{Cond} can be derived from solutions to the one-dimensional heat diffusion equation if the temperature at the top of the permanent cap can be determined throughout the year. Since the polar atmosphere was relatively clear during northern summer when the permanent cap was exposed, the cap's surface temperature can be taken directly from the measured brightness temperatures in the IRTM surface-sensing channels, since water ice is an excellent blackbody emitter. During other seasons, the top of the permanent cap is in direct thermal contact with seasonal CO_2 frost deposits. If the frost deposits are in solid-vapor equilibrium with CO_2 gas in the atmosphere, then their temperatures will not vary with depth, and the temperature at the top of the permanent cap will equal the surface temperature T_s.

The temperatures of Martian CO_2 frost deposits are determined by the local partial pressure of CO_2. In most previous studies, it has been assumed that polar frost deposits lie close to the 6.1 mbar pressure level, giving CO_2 frost temperatures near 148 K. The IRTM observations suggest that the study regions lie somewhat higher. Figures 2A and 3A show that during early fall and late winter, the IRTM brightness temperatures in the available channels were nearly coincident. This occurred in both the north and south study regions and was especially apparent during early fall in the south. The simplest and most likely explanation for this behavior is that the spectral emissivities of seasonal frost deposits in the north and south study regions were very close to unity during these seasons, making the measured brightness temperatures close to actual surface frost temperatures (*9*). Frost temperatures can be used to determine surface CO_2 equilibrium vapor pressures and estimate approximate altitudes for the study regions relative to the 6.1 mbar reference aeroid. With $T_s = 146 \pm 1$ K for the north study region at Julian date 3430 ($L_s = 348.6$) and $T_s = 142 \pm 1$ K for the south study region at Julian date 3490 ($L_s = 18.2$) gives altitudes of $+2.5 \pm 2$ km in the north and $+8 \pm 2$ km in the south assuming a hydrostatic atmosphere of uniform composition with a scale height of 9 km. Although the true uncertainties of these inferred study region elevations are difficult to gauge, they are in good agreement with the general trends displayed by radio occultation altitude determinations at lower latitudes (*17*).

Surface temperatures were calculated for all other seasons in which CO_2 was present by assuming that CO_2 partial surface pressures at the study regions were proportional to the seasonally varying surface pressures measured at Viking Lander 1 (*18*). Figures 2A and 3A show estimated values of T_s for the north and south study regions throughout the year. The day that the north permanent cap was exposed was determined from high emission angle observations that are not shown in Fig. 2A.

With year-long surface temperatures in hand, F_{Cond} can be calculated by treating the north permanent cap as a semi-infinite homogeneous half-space in annual equilibrium. With boundary conditions that surface temperatures equal T_s and that temperature gradients at great depths equal 0 (that is, no heat flow from the Martian interior), the one-dimensional heat diffusion equation was solved to yield F_{Cond} throughout the year (*19*). The solutions are such that the magnitude of F_{Cond} at any given time is proportional to the thermal inertia $I = (k\rho c)^{1/2}$, where k is the thermal conductivity, ρ is the density, and c is the heat capacity of the permanent polar cap material. The thermal inertia of the permanent cap is not expected to exceed 50×10^{-3} cal cm^{-2} · sec$^{1/2}$, the value for solid water ice or rock. Figure 2D shows calculated values for F_{Cond} throughout the year for $I = 10 \times 10^{-3}$, 30×10^{-3}, and 50×10^{-3} cal cm^{-2} · sec$^{1/2}$.

Values for I in the north can be determined from the IRTM observations by considering the heat balance equation during the summer season when the permanent water ice cap is exposed. Since high surface temperatures preclude the stability of solid CO_2 during this season, S_{CO_2} can safely be assumed to be 0 (*9*). This means that Eq. 1 can be solved to yield upper and lower limits for F_{Cond} during northern summer since upper and lower limits for F_{Rad} and values for S_{Atm}

and F_{Horiz} have been determined. Observationally constrained limits for F_{Cond} during northern summer are shown as vertical bars in Fig. 2D. These are consistent with the values of F_{Cond} that were calculated from the heat diffusion equation in the same figure if the thermal inertia of the north permanent cap is in the neighborhood of 30×10^{-3} cal $cm^{-2} \cdot sec^{1/2}$. The goodness of fit provides not only an estimate of the uncertainties in I, but also independent confirmation that possible systematic errors in A_P and $F\uparrow_{IR}$ are not large. The derived inertia applies to the upper few meters of the north permanent cap and is consistent with the notion that it is a coarse-grained or nearly solid admixture of water ice, rock, and dust. Upper and lower limits for calculated year-long values of F_{Cond} for the north study region will be estimated by using permanent cap thermal inertias of 40×10^{-3} and 20×10^{-3} cal $cm^{-2} \cdot sec^{1/2}$.

In the south, the magnitude of F_{Cond} is directly tied to the important question of whether or not solid CO_2 remained on the surface of the south residual cap throughout the summer season. If the entire south study region was covered with solid CO_2 throughout the year, then F_{Cond} would be close to 0. An analysis of the Viking orbiter images of the receding south polar cap suggests that some CO_2 frost may have been left on the outskirts of the residual cap area at the end of summer, but the images alone provide few clues as to the extent of CO_2 cover within the south study region itself toward the end of summer because the rate of change of frost coverage was extremely slow (*4*).

The best evidence for a permanent CO_2 cap in the south has come from Kieffer's analysis of IRTM spring and summer south polar data (*3*). He used observations of the interior of the residual cap at Julian date 3362 (L_s = 311) to estimate that the net flux of solar and infrared radiation at the top of the atmosphere was on the order of 60 W m^{-2}. Kieffer argued that a large fraction of this energy flux must have been going into sublimating surface CO_2 deposits. This result, along with the absence of any unequivocal evidence for an exposed water ice cap in the south [that is, large atmospheric water vapor abundances over the cap (*20*), or any abrupt increases in the IRTM brightness temperatures during late summer] led him to conclude that the south residual cap contained solid CO_2 throughout the first Viking year of observations.

The IRTM observations and heat balance statistics presented here provide additional support for Kieffer's conclusion. It is instructive to observe the behavior of F_{Rad} [the difference between F_{Solar} (1 − A_P) and $F\uparrow_{IR}$] during the early spring seasons when the surfaces of both the north and the south study regions were completely covered with CO_2 frost (Figs. 2C and 3C). As the insolation rate increased in early spring, F_{Rad} underwent a rapid transition from negative to positive values in both the north and the south study regions. Since F_{Cond} is small during this season, this behavior can be readily interpreted as a quick transition from CO_2-condensing to CO_2-sublimating conditions within both study regions. In the south, F_{Rad} stayed positive until late in the summer season and then underwent a rapid transition to negative values as the insolation rate decreased. This behavior is in sharp contrast to the slow transition that was observed in the north and is exactly what would be expected if a large fraction of the surface of the south study region contained sublimating and then condensing CO_2 frost during late summer.

Although CO_2 probably remained throughout the summer in the south, F_{Cond} may not have been exactly 0. During late summer, the surface properties of the south study region were not spatially homogeneous, as judged by the thin lanes of dark unfrosted surface materials that comprised up to 10 percent of the area of the region. Subsurface heat conduction probably played an important role in the local heat balance of these dark areas, but the overall effect of these areas is difficult to assess for two reasons. First, they were not resolved spatially by IRTM, and second, the brightness temperatures in all the surface sensing channels were significantly elevated throughout the spring and summer seasons in the south by thermal emission from dust in the hot south polar atmosphere. Generous upper limits for the magnitude of F_{Cond} during late summer can be estimated by assuming that the exposed areas of the south permanent cap had the thermal inertia of solid water ice and that the average surface temperature of the south study region rose as high as T_{20} during late summer. These assumptions yield upper bounds for F_{Cond} of ±10 W m^{-2}, which are too small to balance F_{Rad} during late summer in the south. This confirms the need for nonzero CO_2 latent heat storage during this season. For the purpose of estimating S_{CO_2} for the south study region, F_{Cond} will be assumed to be 0 throughout the year.

Annual behavior of CO_2 frost. With the necessary terms in the heat balance equations accounted for, it is now possible to present derived CO_2 frost accumulation rates for the north and south study regions during the course of a Martian year. Upper and lower limits for S_{CO_2} for the north study region (Fig. 2D) were computed from Eq. 1 by assuming that the estimated uncertainties in F_{Rad} and F_{Cond} were additive. Upper and lower limits on S_{CO_2} for the south study region (Fig. 3D) reflect uncertainties in F_{Rad} alone.

Before comparing the behavior of CO_2 frost in the north and south, it is important to point out that there is no obvious reason to expect permanent CO_2 frost deposits at only one Martian pole. This is true for elliptical orbits as well as circular ones since the total annual insolation at both poles will always be equal (*17, 21*). Elliptical orbits complicate comparisons between the behavior of CO_2 in the north and south because the durations of seasons and the distributions of incident solar energy within them are not symmetric. Currently, if CO_2 accumulation rates in the absence of sunlight were the same at both poles, then approximately 30 percent more CO_2 would be expected to accumulate in the south during a year because the polar night season there is longer than that in the north. If the properties of the north and south polar surface and atmospheres were identical, then the south's apparent advantage during the fall and winter seasons would be completely canceled out during the spring and summer because the distribution of insolation with time is such that more total sublimation would take place in the south. The results shown in Figs. 2D and 3D are especially useful for understanding the current asymmetric behavior of seasonal frost at the Martian poles because they make it possible to compare the behavior of CO_2 season by season.

On the whole, the north and south study regions behaved symmetrically during their respective fall and winter seasons. Figures 2D and 3D show that the rates of CO_2 condensation within both regions were generally quite comparable during this period except during early northern winter and during the first half of the second global dust storm in the north (*22*). Substituting the upper and lower limits for S_{CO_2} into Eq. 2 and then integrating these rates over the periods in which net frost accumulation occurred yields total annual frost accumulations of 75 ± 12 g cm^{-2} in the north and 110 ± 7 g cm^{-2} in the south for L_{CO_2} = 590 J g^{-1}. Although these derived annual CO_2 accumulations should contain additional uncertainties for F_{Horiz}, they do not sug-

Table 1. Two sets of constraints on the remaining model parameters used in Fig. 5.

Set	Range	$\tilde{\omega}_0$	g	ϵ_s	F_{Horiz} (W m^{-2})	f
1	Minimum	0.84	0.69	0.90	0	0.5
	Maximum	0.88	0.89	1.0	4.0	0.6
2	Minimum	0.4	0.4	0.65	−2.0	0.45
	Maximum	0.99	0.99	1.00	8.0	0.70

gest that the absence of CO_2 frost in the north during summer was primarily due to north-south asymmetries during fall and winter.

The north and south study regions behaved very asymmetrically during their respective spring seasons. Figures 2B, 3B, and 4 show that during late spring, planetary albedos in the south were significantly higher than they were in the north. Comparison between Figs. 2D and 3D shows that by midspring, CO_2 sublimation rates in the north were at least as high as they were in the south despite the fact that insolation rates in the south were over 50 percent greater. Since the north and south study regions experienced similar CO_2 accumulation rates during fall and winter, the absence of permanent CO_2 frost deposits in the north can be primarily attributed to the north study region's ability to convert a significantly greater fraction of its available incident solar energy into CO_2 frost sublimation.

An important question concerning the asymmetric behavior of CO_2 frost at the Martian poles is whether this behavior was primarily due to north-south differences in surface properties, atmospheric properties, or both. It has been suggested that differences in the dust contents of the polar atmospheres or the seasonal frost deposits themselves may play an important role in the asymmetry since global dust storms presently occur only during southern spring and summer and the radiative effects of dust in the atmosphere and on the surface could be large (*7, 23, 24*). The results presented so far have shown that the most important north-south asymmetries occurred during the spring seasons. The next section describes how the observed late spring season heat balance quantities can be interpreted in terms of surface and atmospheric properties with the aid of a polar radiative model.

Polar radiative model. The model described here is similar to the simplified one-dimensional radiative equilibrium model used by Davies to investigate the effects of atmospheric dust on Martian surface and atmospheric heating rates (*24*). By treating the atmosphere's thermal response as instantaneous, the model calculates surface CO_2 sublimation rates and observable radiative fluxes at the top of the atmosphere from an assumed set of aerosol optical properties, surface properties, and atmospheric dynamical heating rates. By comparing the model calculated values of A_P and $F\uparrow_{IR}$ with the observations, the surface and atmospheric properties that are responsible for the contrasting behavior of the north and south study regions during the spring seasons can be identified.

An important task for the model is to calculate the fraction of incident solar energy that is deposited on the surface and in the atmosphere. The planetary albedo, a key observable can be written $A_P = 1 - (H_S + H_A)/F_{Solar}$, where H_S is the surface solar heating rate and H_A is the vertically integrated atmospheric solar heating rate. In the model, the fraction of solar energy absorbed by gaseous CO_2 at near infrared wavelengths is calculated from formulas presented by Pollack *et al.* (*14*). The remaining solar energy (typically 99 percent) is then assumed to be available for broadband multiple scattering and absorption by atmospheric aerosols and the surface. Scattering calculations are performed using a two-stream δ-Eddington code that yields calculated radiative fluxes that are in good agreement with the results of exact solutions to the equation of radiative transfer for the range of aerosol optical properties considered in this paper (*25*). The solar heating rates H_S and H_A are determined by the values of six model parameters: A_s, τ, $\tilde{\omega}_0$, g, F_{Solar}, and φ, where A_s is the solar spectrum averaged surface albedo, τ is the solar spectrum averaged vertical aerosol optical depth or opacity, $\tilde{\omega}_0$ is the solar spectrum averaged aerosol single scattering albedo (*26*), and g is the solar spectrum averaged aerosol scattering phase function asymmetry parameter (*27*).

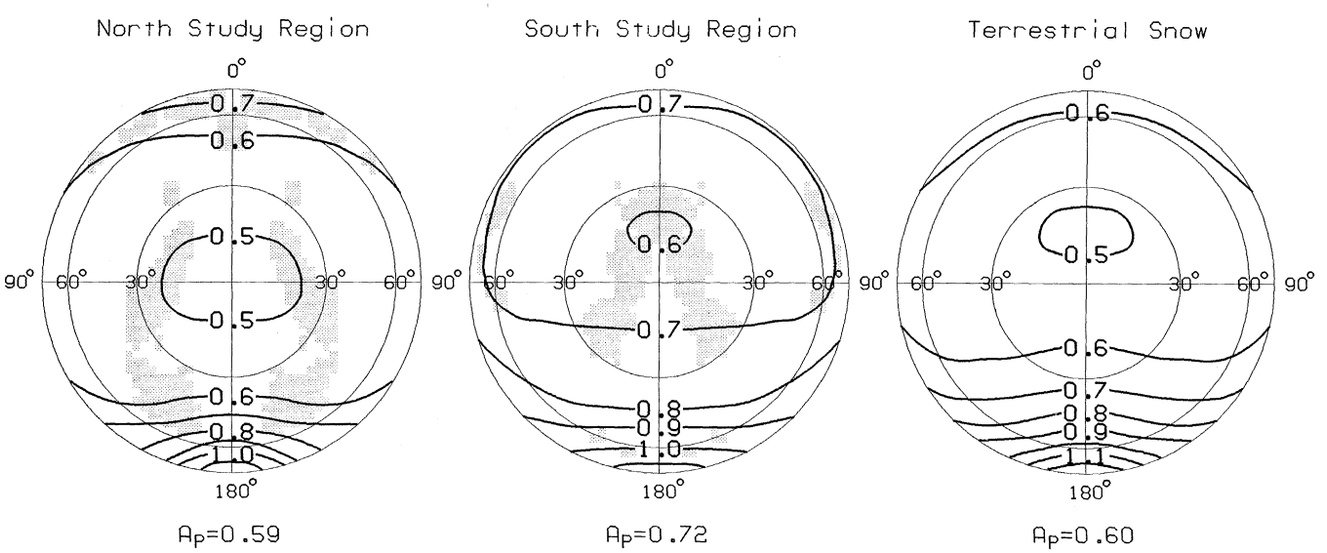

Fig. 4. Bidirectional reflectance plots showing contours of Lambert albedo as a function of emission angle θ (radial) and solar azimuth angle ψ (azimuthal). The sun is at ψ = 0. The IRTM angular coverage is shaded. (Left) North study region, Julian date 3560 to 3630 (L_s 50.0 to 80.7) for solar zenith angles φ of 60° to 70°. (Center) South study region, Julian date 3240 to 3280 (L_s 235.7 to 261.1) for 60° < φ ≤ 70°. (Right) Measured bidirectional reflectance of aged terrestrial snow for φ = 64.1° from (*10*) normalized to A_P = 0.60.

The model's infrared calculations are greatly simplified by the fact that north and south polar atmospheres are in a state of near-thermal equilibrium. Since S_{Atm} is small, and elevated polar atmospheric temperatures preclude the stability of condensed atmospheric CO_2, the model's instantaneous heat balance equation for the atmospheric columns within the study regions during late spring is

$$H_A + F_{Horiz} = F\uparrow_{IR} - \epsilon_s \sigma T_s^4 + \epsilon_s' F\downarrow_{IR}^* \quad (5)$$

where ϵ_s is the Planck weighted average emissivity of the surface frost, σ is the Stefan-Boltzmann constant, $F\downarrow_{IR}^*$ is the downward flux of infrared radiation at the surface, and ϵ_s' is the fraction of $F\downarrow_{IR}^*$ absorbed by the surface (*28*). Equation 5 makes no allowance for vertical convective heat transport between surface and atmosphere because spring season polar atmospheric temperature profiles are very stable. The effects of heat conduction from atmosphere to surface are also small under these circumstances (*13*) and are ignored in this model. The term $F\downarrow_{IR}^*$ is not calculated explicitly in this model but is evaluated in terms of a new free parameter, f, where $f = F\downarrow_{IR}^*/(H_A + F_{Horiz})$; f is a measure of the atmosphere's tendency to reradiate its absorbed solar and dynamically transported energy to the surface. During late spring in the north and south, f should be greater than 0 and less than $(\epsilon_s')^{-1}$ since $(H_A + F_{Horiz})$ is likely to be greater than 0 and $F\uparrow_{IR}$ is greater than $\epsilon_s \sigma T_s^4$ (Eq. 5). A series of more elaborate ten-layer one-dimensional radiative equilibrium model calculations show that f is primarily determined by the vertical distributions of advective heating and aerosol opacity and is relatively insensitive to all other surface and atmospheric properties (*9*). In these calculations, f was found to be greater than 0.45 and less than 0.7 even when all aerosol particles were assumed to be concentrated at the top of the atmosphere or just above the surface. If T_s is known, then $F\uparrow_{IR}$ can be calculated from Eq. 5, given the values of H_S, H_A, F_{Horiz}, f, ϵ_s, and ϵ_s'.

The left and center panels of Fig. 5 show some important aspects of the model's behavior for one of the many possible combinations of inputs to the model. Figure 5 (left panel) shows calculated values of A_P as a function of A_s and τ for $\varphi = 66.5°$, $\tilde{\omega}_0 = 0.86$, and $g = 0.79$. These values for $\tilde{\omega}_0$ and g were derived from analyses of Viking lander imaging observations of the sun and sky (*29*) and are frequently used to characterize the solar spectrum averaged optical properties of Martian dust. The contours in Fig. 5 for A_P show that for this choice of aerosol optical properties, A_P is a lower limit for A_s as long as A_P is greater than 0.3. Also shown are values of S_{CO_2} (Fig. 5, center panel) as a function of A_s and τ for the polar insolation conditions that occur during late southern spring; S_{CO_2} can be determined from model calculated values of A_P and $F\uparrow_{IR}$ in Eq. 3 with the assumption that $F_{Cond} = 0$ in Eq. 1. Other values used were $F_{Solar} = 290.7$ W m^{-2}, $\varphi = 66.5°$, $\tilde{\omega}_0 = 0.86$, $g = 0.79$, $T_s = 142.5$ K, $\epsilon_s' = \epsilon_s = 1$, $F_{Horiz} = 2$ W m^{-2}, and $f = 0.55$. The contours for S_{CO_2} support Davies' conclusion that the addition of atmospheric dust can either result in increased or decreased surface sublimation rates depending on the surface albedo, but also show that spring season surface CO_2 sublimation rates are much stronger functions of A_s than of τ. This strong dependence makes A_s both the most important and the most confidently inferable property of the study regions during spring.

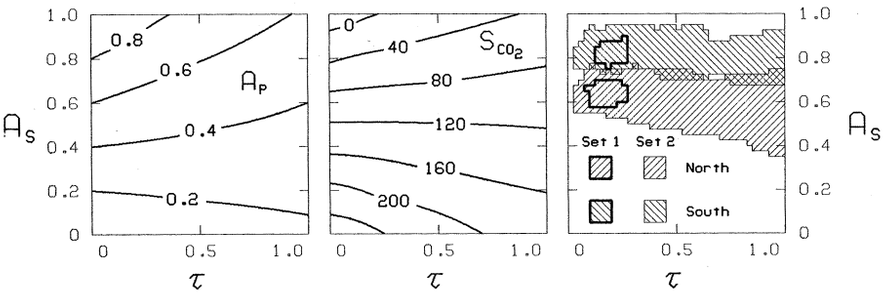

Fig. 5. (Left) Calculated spring season planetary albedos A_P and (center) south study region surface CO_2 latent heat storage rates S_{CO_2} as a function of surface albedo A_s and dust opacity τ for one combination of model input parameters. (Right) Inferred surface albedos and aerosol opacities for the north study region at Julian date 3595 ($L_s = 65.4$) and for the south study region at Julian date 3265 ($L_s = 251.6$) for all combinations of two sets of model parameters.

An extensive set of model calculations were performed for the insolation conditions at Julian date 3265 ($L_s = 251.6$) for the south study region and Julian date 3595 ($L_s = 65.4$) for the north study region (arrows at the top in Figs. 2A and 3A). These particular dates were chosen for comparing the model results with the IRTM observations for a number of reasons. First, insolation rates at the top of the atmosphere in the north and south were near their maximum values with average solar zenith angles near 66.5° for both study regions. Second, the Viking orbiter images show that the surfaces of both study regions were plainly visible and completely covered with seasonal CO_2 frost (*4, 30*). Also, the diameters of both seasonal polar caps were approximately 20° of latitude, and the planetary albedos of both regions were well constrained. On these dates, observed upward infrared fluxes at the top of the atmosphere in the north and south were similar while observed planetary albedos at the top of the atmosphere in the south were distinctly higher ($0.54 \leq A_P \leq 0.62$ and $32.0 \leq F\uparrow_{IR} \leq 35.6$ for the north study region, $0.69 \leq A_P \leq 0.77$ and $35.3 \leq F\uparrow_{IR} \leq 42.0$ for the south region).

The calculations were performed by varying each of the inputs to the model, A_s, τ, g, F_{Horiz}, ϵ_s, and f, over a wide range in every possible combination and then recording only those combinations of parameters that yielded model calculated values of A_P and $F\uparrow_{IR}$ that were within their measured upper and lower limits on the chosen dates in the north and the south (*31*). Table 1 shows two sets of constraints on the parameters $\tilde{\omega}_0$, g, F_{Horiz}, ϵ_s, and f. The first set covers a likely range of dust optical properties and study region surface and atmospheric properties. The second set covers a much wider range, including nearly all possible water ice, dust, and soot optical properties and a very wide range of study region surface and atmospheric properties. Figure 5 (right panel) shows all combinations of A_s and τ that yielded calculated values of A_P and $F\uparrow_{IR}$ that were within their measured upper and lower limits when the two sets of constraints on the model parameters in Table 1 were imposed. The calculations show that the late spring season IRTM observations are consistent with the first set of constraints only if dust opacities in the north and south are similar and surface frost albedos in the south are distinctly higher. When the wider ranging second set of constraints are used, the observations still require surface frost albedos in the south to be higher than those in the north for almost every combination as long as τ is less than 1.0. This last condition is guaranteed by the Viking orbiter images of the study regions during these seasons.

Discussion. It appears then that the

contrasting behavior of CO_2 frost at the north and south poles of Mars during the Viking year can be attributed almost entirely to spring season surface frost albedos being approximately 25 percent lower in the north than in the south. Experience from terrestrial snow and water ice studies has shown that albedo variations of this magnitude can arise from variations in frost microphysical properties such as grain size and from variations in the concentrations of absorbing contaminants such as dust (*32*). In view of the extreme sensitivity of pure frost reflectivities to the addition of minute quantities of absorbing materials (*33*) and the ready supply of dust in the Martian atmosphere, preferential dust contamination of the seasonal frost deposits that overlie the north residual cap seems a very likely explanation for the behavior and properties discussed above.

If dust contamination is responsible for the lower reflectivities of the seasonal frost deposits at the north pole, then it will be important to establish whether this contamination occurs primarily during global dust storms in the fall and winter or during local dust storms at the cap edge in early spring (*34*). If global dust storms are primarily responsible, then the north permanent cap should become exposed much later in the season during years in which no global dust storms occur.

In the south, the high surface albedos that are inferred during late spring are puzzling in that they suggest that the exposed seasonal frost deposits within the south study region contained no significant quantities of dust despite the occurrence of a major global dust storm earlier in the season. In addition, the results shown in Figs. 3B and 3D suggest that the south study region surface albedos continued to be high even during the second global dust storm of 1977, as shown by the sharp rebound in planetary albedos and the continued low surface CO_2 sublimation rates after the initial intense phase of the storm. Understanding exactly how the seasonal frost deposits at the south residual cap are able to maintain their high reflectivities through the dusty spring and summer seasons could be very important since the vapor pressures of these deposits could well be determining the present mass of the Martian atmosphere.

The Viking results have made it clear that the annual heat balance at the Martian poles is not a purely local phenomenon, but may be strongly influenced by the complex, global scale geologic and atmospheric processes that bring dust to the polar regions each year. In 1991, the Mars Observer is scheduled to arrive at Mars, enter into a low polar orbit, and begin surveying its surface, atmosphere, and magnetosphere for one Mars year. By better defining the global circulation of dust in the Martian atmosphere, the surface topography of the Martian polar regions, and the behavior and properties of Martian CO_2 frosts on the surface and in the atmosphere, the Mars Observer may help provide a new and more detailed understanding of the Martian polar caps and their relation to the Martian climate.

References and Notes

1. H. H. Kieffer, S. C. Chase, E. D. Miner, F. D. Palluconi, *Science* **194**, 1341 (1976).
2. C. B. Farmer, D. W. Davies, D. D. La Porte, *ibid.*, p. 1339.
3. H. H. Kieffer, *J. Geophys. Res.* **84**, 4249 (1976).
4. P. B. James, G. Briggs, J. Barnes, A. Spruck, *ibid.*, p. 2889.
5. R. B. Leighton and B. C. Murray, *Science* **153**, 136 (1966).
6. When the annual heat balance at both poles does not favor the stability of permanent CO_2 deposits, the Martian atmosphere may then be in equilibrium with a large reservoir of CO_2 adsorbed onto minerals in a thick, porous, planetwide rubble layer known as the Martian regolith [F. P. Fanale *et al.*, *Icarus* **50**, 381 (1982)].
7. O. B. Toon *et al.*, *ibid.* **44**, 552 (1980).
8. The design and operation of the IRTM's are more completely described by H. H. Kieffer *et al.* [*J. Geophys. Res.* **82**, 4249 (1977)] and S. C. Chase *et al.* [*Appl. Opt.* **17**, 1243 (1978)].
9. D. A. Paige, thesis, California Institute of Technology, Pasadena (1985).
10. I. Dirmhirn and F. D. Eaton, *J. Appl. Meteorol.* **14**, 275 (1975).
11. J. T. Houghton, *The Physics of Atmospheres* (Cambridge Univ. Press, Cambridge, 1977), pp. 20–22.
12. The total potential energy of the atmosphere within the boundaries of the study regions also underwent seasonal variations due to changes in the mass of the Martian atmosphere caused by the global condensation and sublimation of CO_2 frost (*19*). Although changes in total atmospheric potential energy due to these seasonal mass variations were of the same order as those due to seasonal temperature variations, the mass variations were not used to estimate S_{Atm} because they were likely to have been balanced during most seasons by equivalent variations in F_{Horiz} with no strong direct effects on S_{CO_2}.
13. C. B. Leovy and Y. Mintz, *J. Atmos. Sci.* **26**, 1167 (1969).
14. J. B. Pollack *et al.*, *ibid.* **38**, 3 (1981).
15. Similar advective heating rates are required by a one-dimensional radiative-dynamic equilibrium model to explain the IRTM 15-μm channel observations of the north and south study regions during the fall and winter seasons (*9*).
16. The assumption is independent of the mode of heat transport to the poles, which may be entirely by atmospheric gases or may possibly include a contribution from the latent heat contained in wind blown frost [P. J. Thomas *et al.*, *J. Geophys. Res.* **84**, 4621 (1979)].
17. B. C. Murray and M. C. Malin, *Science* **182**, 437 (1973).
18. S. L. Hess *et al.*, *Geophys. Res. Lett.* **7**, 197 (1980).
19. H. S. Carslaw and J. C. Jaeger, *Conduction of Heat in Solids* (Oxford Univ. Press, Oxford, 1959), pp. 50–83 and p. 497.
20. D. W. Davies and L. A. Wainio, *J. Geophys. Res.* **84**, 216 (1979).
21. R. W. Ward, B. C. Murray, M. C. Malin, *ibid.* **79**, 3187 (1974).
22. The elevated rates of CO_2 condensation that are inferred during the first part of the storm could well be an artifact of the assumption that F_{Horiz} remained constant throughout the year [T. Z. Martin and H. H. Kieffer, *ibid.* **84**, 2843 (1979)]. Upward heat conduction from the permanent cap played an important role in the heat balance of the north study region during fall as a large fraction of F_{Cond} probably resulted in CO_2 frost sublimation at the base of the accumulation seasonal frost layer. Since the net vertically integrated rates of CO_2 condensation within the north and south study regions were comparable, CO_2 accumulation rates at the top of the seasonal frost layer in the north must have been slightly higher than they were in the south. Higher combined surface and atmospheric CO_2 condensation rates are not unexpected in the north because of its lower elevation.
23. H. H. Kieffer and F. D. Palluconi, *NASA Conf. Publ. 2072* (1979).
24. D. W. Davies, *J. Geophys. Res.* **84**, 8289 (1979).
25. H. J. Joseph, W. J. Wiscomb, J. A. Weinman, *J. Atmos. Sci.* **33**, 2452 (1976).
26. $\tilde{\omega}_0$ is the ratio of scattered to scattered and absorbed radiation in a single scattering event; $\tilde{\omega}_0$ equals 1 for nonabsorbing particles.
27. g is the difference between the fractions of singly scattered radiation redirected into the forward and rearward hemispheres; g equals 0 for isotropic scattering and 1 for totally forward scattering.
28. ϵ_s' and ϵ_s are not the same quantities because the spectral distributions of the downward infrared fluxes and the upward emitted fluxes at the surface are not necessarily the same.
29. J. B. Pollack *et al.*, *J. Geophys. Res.* **84**, 2929 (1979).
30. J. A. Cutts, K. R. Blausius, J. Roberts, *ibid.*, p. 2975.
31. ϵ_s' was assumed to equal ϵ_s for all calculations.
32. S. G. Warren and W. J. Wiscomb, *J. Atmos. Sci.* **37**, 2734 (1980).
33. R. N. Clark, *Icarus* **49**, 244 (1982).
34. R. W. Zurek, *ibid.* **50**, 288 (1982).

35. We thank all those who contributed to the great success of the Viking project, with special thanks to H. H. Kieffer, F. D. Palluconi, and R. W. Zurek for encouragement and assistance. Contribution 4148, Division of Geological and Planetary Sciences, California Institute of Technology.